

Shallow, gravity-driven flow in a poro-elastic layer

Duncan R. Hewitt^{1,2,†}, Jerome A. Neufeld^{1,3,4} and Neil J. Balmforth²

¹Department of Applied Mathematics and Theoretical Physics, University of Cambridge, Cambridge CB3 0WA, UK

²Department of Mathematics, University of British Columbia, Vancouver, BC, Canada V6T 1Z2

³Department of Earth Science, University of Cambridge, Cambridge CB3 0EZ, UK

⁴BP Institute, University of Cambridge, Cambridge CB3 0EZ, UK

(Received 5 January 2015; revised 15 May 2015; accepted 23 June 2015;
first published online 5 August 2015)

By combining Biot's theory of poro-elasticity with standard shallow-layer scalings, a theoretical model is developed to describe axisymmetric gravity-driven flow through a shallow deformable porous medium. Motivated in part by observations of surface uplift around CO₂ sequestration sites, the model is used to explore the injection of a dense fluid into a horizontal, deformable porous layer that is initially saturated with another, less dense, fluid. The layer lies between a rigid base and a flexible overburden, both of which are impermeable. As the injected fluid spreads under gravity, the matrix deforms and the overburden lifts up. The coupled model predicts the location of the injected fluid as it spreads and the resulting uplift of the overburden due to deformation of the solid matrix. In general, the uplift spreads diffusively far ahead of the injected fluid. If fluid is injected with a constant flux and the medium is unbounded, both the uplift and the injected fluid spread in a self-similar fashion with the same similarity variable $\propto r/t^{1/2}$. The asymptotic form of this spreading is established. Results from a series of laboratory experiments, using polyacrylamide hydrogel particles to create a soft poro-elastic material, are compared qualitatively with the predictions of the model.

Key words: geophysical and geological flows, gravity currents, porous media

1. Introduction

Gravity currents and other shallow flows through porous media play a central role in a range of geophysical and industrial problems, ranging from the seepage of contaminated plumes or the spread of fresh water lenses above saline aquifers to the displacement of one fluid by another in oil reservoirs to enhance recovery (Bear 1988; Phillips 2009). The fluid mechanics of such flows are often explored under the assumption that the porous matrix does not deform due to fluid flow. However, when flow-induced pressure gradients are high, or when the solid matrix is relatively soft,

† Email address for correspondence: drh39@cam.ac.uk

as in some biological problems (e.g. Mow, Holmes & Lai 1984), the deformation of the matrix can be significant. Our goal in the current paper is to formulate a model of poro-elastic flow in a shallow layer, where elastic deformation of the porous matrix is coupled to the flow of fluid through it. We apply the model to study the dynamics of axisymmetric poro-elastic gravity currents.

Specific motivation for this problem comes from observations of surface displacements at the CO₂ storage sites at In Salah in the Algerian desert (Ringrose *et al.* 2013). Geological sequestration has been widely proposed as a means of countering atmospheric emissions of CO₂ through the injection of supercritical CO₂ into (typically) water-saturated porous rock (e.g. Zhang 2013; Huppert & Neufeld 2014). Being less dense than the ambient water, injected CO₂ rises and spreads as a gravity current below the impermeable overburden of the porous reservoir (Boait *et al.* 2012). At In Salah, approximately 4 million tonnes of CO₂ were sequestered between 2004 and 2011 into a sandstone layer, roughly 20 m thick and located approximately 2 km underground (Ringrose *et al.* 2009, 2013). Around the sites of injection, vertical surface displacements of the order of centimetres have been detected by interferometric synthetic aperture radar (InSAR) measurements (Onuma & Ohkawa 2009; Rucci, Vasco & Novali 2013). These observations highlight how the injection and subsequent spread of CO₂ has deformed the porous sandstone layer, much as fluid pumping in other hydrological contexts generates subsidence or uplift (e.g. Bear & Corapcioglu 1981*a,b*). The InSAR measurements have been proposed as a monitor of the progress of the CO₂ current (Ringrose *et al.* 2009), even though the detailed relation between the uplift at the surface and the location of the underlying current has not yet been fully understood.

The large horizontal and thin vertical extent that is typical of sequestration sites is well suited to the conventional shallow-layer modelling of gravity currents (e.g. Huppert & Woods 1995; Lyle *et al.* 2005; Nordbotten & Celia 2006). Despite this, most existing studies in geological engineering use standard geomechanical models coupled with reservoir-type simulations (Rutqvist, Vasco & Myer 2010; Bissell *et al.* 2011; Rutqvist 2012). These studies have provided predictions for uplift and rates of spread that have been compared with the observations from In Salah, highlighting how local topography and fractures have helped to guide the flow of CO₂. They do not, however, focus on the detailed fluid mechanics of spreading poro-elastic currents, nor extract the dependence on the physical parameters of the problem, which are the goals of the current paper.

In this paper we formulate a poro-elastic model for axisymmetric flow in a shallow layer that combines Biot's theory (e.g. Detournay & Cheng 1993; Coussy 2004) with shallow-layer scalings following standard gravity-current theory (e.g. Huppert & Woods 1995). Our methodology is similar to that adopted for other subsidence and pumping problems in hydrology (e.g. Gibson, Schiffman & Pu 1970; Bear & Corapcioglu 1981*a,b,c*) and industrial filtration (Barry, Mercer & Zoppou 1997). In a biological context, a similar poro-elastic framework has been used to describe cell dynamics (Charras, Mitchison & Mahadevan 2009; Moendarbary *et al.* 2013) and tissue swelling or oedemas (Simon *et al.* 1996). Indeed, flow-induced deformation of shallow poro-elastic layers is central to a number of biological problems, with the indentation of tissue layers such as cartilage playing a key role in, for example, the lubrication of joints (see Mak, Lai & Mow 1987; Mow *et al.* 1989; Jensen *et al.* 1994; Sachs *et al.* 1994; Barry & Holmes 2001).

Our current formulation generalizes previous models in two notable ways: first, we allow for two fluids of different density, one displacing the other as it spreads under gravity (we assume that the medium is fully saturated). Second, we assume that the poro-elastic layer lies between a rigid base and a flexible overburden, both of which are impermeable, and that the poro-elastic material cannot slide freely at either surface. Poro-elastic deformations are therefore significantly constrained by the shallow geometry. Both features provide the conceptual framework for application to uplift in CO₂ sequestration.

We complement our theoretical model with a series of idealized laboratory experiments. Previous experimental studies using deformable media have predominantly been concerned with one-dimensional compression tests, using materials such as artificial sponges (Parker, Mehta & Caro 1987; Lanir, Saub & Maretsky 1990), synthetic fibres (Barabadi *et al.* 2009) and biological tissue (Eisenberg & Grodzinsky 1987). In more recent experiments, MacMinn, Dufresne & Wettlaufer (2015) used a mono-layer of small spherical polyacrylamide hydrogel particles to study flow-induced deformation of an idealized two-dimensional poro-elastic medium. Such hydrogels are convenient materials for poro-elastic experiments, being relatively inexpensive and straightforward to prepare and visualize. We used similar hydrogel particles, fully saturated in water, to provide a rough experimental analogue of the theoretical model.

The paper is laid out as follows. In §2, we formulate the poro-elastic shallow-layer framework to construct our model. The model takes the form of coupled evolution equations for the height of the injected fluid current and the uplift of the flexible overburden owing to deformation of the medium. In §3, we discuss numerical results of the model with a constant flux of injection. In §4, we present an asymptotic analysis of the model and deduce scaling relationships for the spread of the injected current and of the uplift. In §5, we present the results of the laboratory experiments. The main conclusions and implications of this work are summarized in §6.

2. Theoretical modelling

2.1. Governing equations

We consider flow through a deformable porous medium in an axisymmetric geometry described by cylindrical polar coordinates (r, z) (figure 1). The porous layer sits on top of a rigid, impermeable, flat base located at $z = 0$ and extends up to a height $z = H(r, t)$, where it is overlain by a heavy flexible sheet. The layer initially has uniform depth $H = H_0$. The solid matrix has constant density ρ_s , and the medium is initially fully saturated with ambient fluid of density $\rho_2 \leq \rho_s$ and viscosity μ_2 . Another fluid of density ρ_1 and viscosity μ_1 is injected into the medium and spreads under gravity. Following standard gravity-current theory (Huppert & Woods 1995), we take $\rho_1 \geq \rho_2$, so that the injected fluid spreads along the bottom of the porous layer; the spreading of a lighter fluid injection along the top of the medium can be modelled in an analogous fashion. The interface between the two fluids is denoted by $z = h(r, t)$. The amount of fluid within a representative volume element of the material is given by the porosity $\phi(r, z, t)$, which varies in both space and time. The pore-averaged velocity of the fluid and solid phases are $\mathbf{u}_f = (u_f, w_f)$ and $\mathbf{u}_s = (u_s, w_s)$, respectively. Both phases are assumed to be incompressible, such that their densities are constant.

The governing equations for flow and deformation in a poro-elastic medium are continuity for the liquid and the solid phases, Darcy's law and a global momentum balance:

$$\frac{\partial \phi}{\partial t} + \nabla \cdot (\phi \mathbf{u}_f) = 0, \quad \frac{\partial}{\partial t} (1 - \phi) + \nabla \cdot [(1 - \phi) \mathbf{u}_s] = 0, \quad (2.1a, b)$$

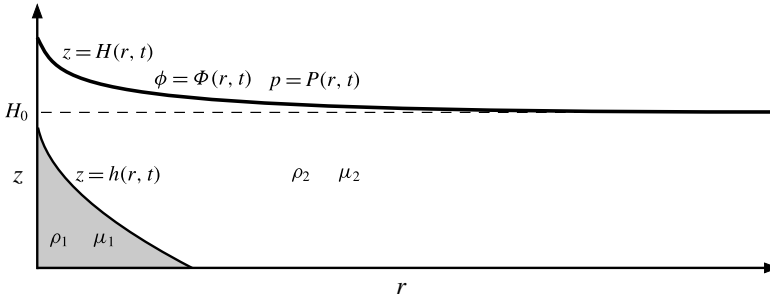


FIGURE 1. A schematic showing the depth $h(r, t)$ of the injected fluid and the uplift $H(r, t)$ of the overburden, associated with an injected flux Q at $r=0$. The porosity and fluid pressure at $z=H$ are given by $\phi = \Phi(r, t)$ and $p = P(r, t)$, respectively. Before any fluid is injected, $H = H_0$, $\Phi = \Phi_0$ and $P = \mathcal{P}$, where \mathcal{P} is the overburden pressure.

$$\phi(\mathbf{u}_f - \mathbf{u}_s) = -\frac{k}{\mu_i}(\nabla p + \rho_i g \mathbf{e}_z), \tag{2.2}$$

$$\nabla \cdot [(1 - \phi)\boldsymbol{\sigma} - \phi p \mathbf{I}] = [\rho_i \phi + \rho_s(1 - \phi)]g \mathbf{e}_z, \tag{2.3}$$

where $k(\phi)$ is the permeability of the medium, p is the pore pressure, g is the gravitational acceleration, $\boldsymbol{\sigma}$ is the phase-averaged solid stress tensor, \mathbf{I} is the identity tensor and \mathbf{e}_z is the unit vector in the z direction. The subscript i refers to the injected ($i = 1$) or ambient ($i = 2$) fluid.

The equations are closed by a constitutive law for the solid stress. More commonly, as suggested by Terzaghi’s principle in soil mechanics (e.g. Wang 2000), the closure is a constitutive law for the ‘effective’ stress tensor $\boldsymbol{\sigma}_e$ of the medium, which is the difference between the total volume-averaged stress and the pore pressure, $\boldsymbol{\sigma}_e = (\boldsymbol{\sigma} + p\mathbf{I})(1 - \phi)$. The momentum balance (2.3) can be re-written in terms of $\boldsymbol{\sigma}_e$ as

$$\nabla \cdot (\boldsymbol{\sigma}_e - p\mathbf{I}) = [\rho_i \phi + \rho_s(1 - \phi)]g \mathbf{e}_z. \tag{2.4}$$

In general, an elastic constitutive law for $\boldsymbol{\sigma}_e$ takes the form

$$\boldsymbol{\sigma}_e = \boldsymbol{\sigma}_e(\nabla \boldsymbol{\xi}), \tag{2.5}$$

where $\boldsymbol{\xi} = (\xi, \zeta)$ is the deformation of the medium away from a reference state with constant porosity Φ_0 . The deformation, which we describe in terms of Eulerian variables, is related to the solid velocity \mathbf{u}_s via the convective derivative

$$\mathbf{u}_s = \left(\frac{\partial}{\partial t} + \mathbf{u}_s \cdot \nabla \right) \boldsymbol{\xi}. \tag{2.6}$$

In this paper, following standard formulations of Biot’s theory (e.g. Detournay & Cheng 1993), we adopt a linear elastic constitutive law (i.e. Hooke’s law) for the effective stress (2.5),

$$\boldsymbol{\sigma}_e = \left(K - \frac{2}{3}G \right) (\nabla \cdot \boldsymbol{\xi})\mathbf{I} + G[(\nabla \boldsymbol{\xi}) + (\nabla \boldsymbol{\xi})^T], \tag{2.7}$$

where K and G are the bulk and shear moduli, which are assumed to be constant. Note that these moduli are properties of the porous medium, rather than of the pure solid alone. In fact, in the shallow-layer limit introduced in § 2.2, (2.7) simplifies significantly and could be replaced by a more general nonlinear constitutive law without undue extra complication.

2.2. Dimensionless shallow-layer scalings

We suppose that the vertical extent H_0 of the porous layer is much less than the characteristic radial length scale L of the flow, so that $H_0 \ll L$. Scaling analysis of the continuity equation for the fluid phase (2.1a) indicates that $w_f \ll u_f$. However, we cannot make the same deduction for the solid velocity in (2.1b): under the assumption that the solid cannot freely slip on the boundaries, there must be a frictional balance between normal and shear stress there, which indicates that $\xi \sim \zeta$ and thus $u_s \sim w_s$. The relative magnitude of the fluid and solid velocities can be determined by (2.1), which indicates that $w_s \sim w_f$, and so $u_s \ll u_f$.

We introduce the following dimensionless quantities:

$$r^* = \frac{r}{L}, \quad (z^*, \xi^*, \zeta^*) = \frac{1}{H_0}(z, \xi, \zeta), \quad \rho_i^* = \frac{\rho_i}{\rho_s}, \quad p^* = \frac{p}{\rho_s g H_0}, \quad k^* = \frac{k}{k_0}, \quad (2.8a-e)$$

$$u_f^* = \frac{u_f}{U}, \quad (w_f^*, u_s^*, w_s^*) = \frac{L}{UH_0}(w_f, u_s, w_s), \quad t^* = \frac{Ut}{L}, \quad (2.9a-c)$$

where $U = \rho_s g k_0 H_0 / \mu_1 L$ and $k_0 = k(\Phi_0)$ is a characteristic permeability scale. For notational convenience, we also define the scaled dimensionless density differences and the viscosity, or mobility, ratio,

$$\hat{\rho}_1 = (1 - \Phi_0) \frac{\rho_s - \rho_1}{\rho_s}, \quad \hat{\rho}_2 = (1 - \Phi_0) \frac{\rho_s - \rho_2}{\rho_s}, \quad (2.10a,b)$$

$$\Delta\rho = \frac{\rho_1 - \rho_2}{\rho_s} = \hat{\rho}_2 - \hat{\rho}_1, \quad M = \frac{\mu_1}{\mu_2}. \quad (2.11a,b)$$

For the arrangement depicted in figure 1, $0 \leq \hat{\rho}_1 \leq \hat{\rho}_2 \leq 1$ and $\Delta\rho \geq 0$. At this stage, the radial length scale L is not prescribed by the dynamics, and in the absence of an external radial scale in the boundary conditions it remains undetermined. In such a situation, we expect that the equations permit a similarity solution, as we in fact find to be the case and discuss in § 3.

In the shallow-layer framework, we retain only the leading-order terms in H_0/L . The dimensionless shallow-layer continuity equations are given from (2.1) by

$$\frac{\partial \phi}{\partial t^*} = -\frac{1}{r^*} \frac{\partial}{\partial r^*}(r^* \phi u_f^*) - \frac{\partial}{\partial z^*}(\phi w_f^*) = \frac{\partial}{\partial z^*}[(1 - \phi)w_s^*]. \quad (2.12a,b)$$

From (2.2) and the shallow-layer scalings, the pore pressure is hydrostatic and the fluid velocity is given by the horizontal component of Darcy’s law,

$$\frac{\partial p^*}{\partial z^*} = -\rho_i^*, \quad \phi u_f^* = \begin{cases} -k^* \partial p^* / \partial r^* & \text{for } 0 < z^* < h^*, \\ -Mk^* \partial p^* / \partial r^* & \text{for } h^* < z^* < H^*. \end{cases} \quad (2.13a,b)$$

The vertical momentum balance in (2.4), together with the linearly elastic rheology (2.7), reduces to an ordinary differential equation for the vertical displacement ζ^* , given by

$$E \frac{\partial^2 \zeta^*}{\partial z^{*2}} - \frac{\partial p^*}{\partial z^*} = [\rho_i^* \phi + (1 - \phi)], \quad (2.14)$$

where

$$E = \frac{K + 4G/3}{\rho_s g H_0} \tag{2.15}$$

is a dimensionless elastic modulus or stiffness of the medium.

In the shallow framework, the closure relationship (2.6) becomes one-dimensional and gives an explicit equation for the solid velocity: $w_s^* = \partial \zeta^* / \partial t^* / (1 - \partial \zeta^* / \partial z^*)$. Substitution of this expression into the equation of continuity of the solid phase (2.12*b*) gives, after rearranging,

$$\left(\frac{\partial}{\partial t^*} + w_s^* \frac{\partial}{\partial z^*} \right) \left(\frac{1 - \partial \zeta^* / \partial z^*}{1 - \phi} \right) = 0, \tag{2.16}$$

or, after integration,

$$\frac{\partial \zeta^*}{\partial z^*} = \frac{\phi - \Phi_0}{1 - \Phi_0} \tag{2.17}$$

given that Φ_0 is the constant porosity of the reference state. Equations (2.13*a*), (2.14) and (2.17) can be combined to eliminate ζ^* and p^* :

$$\frac{\partial \phi}{\partial z^*} = \frac{\hat{\rho}_i (1 - \phi)}{E}. \tag{2.18}$$

The horizontal deformation ξ^* does not appear in the equations given above, which is a result of the linear elastic constitutive law (2.7). For a more general nonlinear constitutive law, the leading-order elastic stress might also feature the strain component $\partial \xi / \partial z$, which could be recovered from the leading-order horizontal stress balance in (2.4).

2.3. Boundary and initial conditions

For the remainder of the paper, we drop the starred notation that identifies the dimensionless variables.

2.3.1. Surface and interface conditions

The boundary conditions on the impermeable and immobile base of the medium are

$$w_f = w_s = \zeta = 0 \quad \text{at } z = 0, \tag{2.19}$$

while the interface $z = h(r, t)$ between the two fluids satisfies the kinematic condition

$$\frac{\partial h}{\partial t} + u_f|_{z=h} \frac{\partial h}{\partial r} = w_f|_{z=h}. \tag{2.20}$$

At the upper surface of the medium, we assume that both the solid and the fluid phases remain in contact with the overburden at all times. In the shallow-layer limit, the corresponding kinematic conditions are

$$\frac{\partial H}{\partial t} + u_f|_{z=H} \frac{\partial H}{\partial r} = w_f|_{z=H} \quad \text{and} \quad \frac{\partial H}{\partial t} = w_s|_{z=H}. \tag{2.21a,b}$$

A balance of normal stress at the upper surface of the medium also gives

$$-p + \mathbf{e}_z \cdot \boldsymbol{\sigma}_e \cdot \mathbf{e}_z = -\mathcal{P} \quad \text{at } z = H, \tag{2.22}$$

where \mathcal{P} is the dimensionless normal stress imposed by the overburden. Given the constitutive equation (2.7) and the shallow-layer scalings, we have $\mathbf{e}_z \cdot \boldsymbol{\sigma}_e \cdot \mathbf{e}_z = E\partial\zeta/\partial z$, and so, from (2.17), the normal-stress balance reduces to

$$p - \mathcal{P} = E \frac{\phi - \Phi_0}{1 - \Phi_0} \quad \text{at } z = H. \tag{2.23}$$

The stress \mathcal{P} in general contains contributions from the bending and tension of the overburden, as well as from gravity. Here, we neglect the elastic response of the overburden and take \mathcal{P} to be a constant, given by the weight of the overburden per unit area.

2.3.2. Injection and far-field conditions

Fluid is injected into the medium as a point source at the origin with a flux $Q(t)$, while no ambient fluid is removed. Thus,

$$\lim_{r \rightarrow 0} \int_0^h r \phi u_f \, dz = \frac{Q}{2\pi}, \quad \lim_{r \rightarrow 0} \int_h^H r \phi u_f \, dz = 0, \tag{2.24a,b}$$

where we note that the dimensional flux is $QH_0LU = Q\rho_s g k_0 H_0^2 / \mu_1$.

For the analysis of the model, we assume that the domain extends infinitely in the radial direction with

$$h \rightarrow 0, \quad H \rightarrow 1, \quad \text{as } r \rightarrow \infty. \tag{2.25a,b}$$

For laboratory experiments and numerical computations the extent of the domain must be finite. In these cases, we consider an impermeable boundary where $\partial H/\partial r = \partial h/\partial r = 0$ at $r = r_{edge} \gg 1$. We will be primarily interested in times before significant pressure signals from the injection have reached the edge of the domain, and so this far-field boundary condition plays little role in the dynamics.

2.3.3. Initial conditions

The medium has initial depth $H(r, t = 0) = 1$, and is fully saturated with ambient fluid such that $h(r, t = 0) = 0$. The initial porosity profile $\phi(r, z, t = 0) = \phi_0(z)$ can be calculated from the integral of (2.18), and is given by

$$\phi_0 = 1 - (1 - \Phi_0)e^{(1-z)\hat{\rho}_2/E}, \tag{2.26}$$

where we have fixed the reference state $\phi(t = 0, z = 1) = \Phi_0$ to coincide with the initial condition at the surface. Note that if the stiffness E is sufficiently small, (2.26) unphysically predicts that the porosity falls below zero at a finite depth within the layer. In a physical setting, it is likely that the assumption of linear elasticity would break down well before this limit is reached. In practice, we will only consider parameter settings in which the porosity is everywhere significantly larger than zero, and so we ignore the possibility of vanishing porosity.

2.4. *The dimensionless model*

By integrating (2.13a), we find that the hydrostatic pore pressure is

$$p(r, z, t) = \begin{cases} P + \rho_2(H - h) + \rho_1(h - z) & \text{for } 0 < z < h, \\ P + \rho_2(H - z) & \text{for } h < z < H, \end{cases} \quad (2.27)$$

where $P(r, t)$ is the (unknown) surface pore pressure. The porosity distribution is given by integrating (2.18), which yields

$$\phi(r, z, t) = \begin{cases} 1 - (1 - \Phi)e^{(H-h)\widehat{\rho}_2/E+(h-z)\widehat{\rho}_1/E} & \text{for } 0 < z < h, \\ 1 - (1 - \Phi)e^{(H-z)\widehat{\rho}_2/E} & \text{for } h < z < H, \end{cases} \quad (2.28)$$

where $\Phi(r, t)$ is the porosity at $z = H$. The pressure P and porosity Φ are linked by the continuity of normal stress at $z = H$ (2.23), which gives

$$P - \mathcal{P} = E \frac{\Phi - \Phi_0}{1 - \Phi_0}. \quad (2.29)$$

The porosity Φ at the upper surface is also related to the heights h and H via the kinematic condition (2.21), which can be combined with the vertical integral of the continuity equations (2.12) to give a conservation law for the solid phase in any vertical slice,

$$\frac{\partial}{\partial t} \left[\int_0^H (1 - \phi) dz \right] = 0, \quad \text{or} \quad \int_0^H (1 - \phi) dz = \int_0^1 (1 - \phi_0) dz. \quad (2.30a,b)$$

Using (2.26) and (2.28), we then find the following expression for the surface porosity $\Phi[h(r, t), H(r, t)]$:

$$\frac{1 - \Phi}{(1 - \Phi_0)[e^{\widehat{\rho}_2/E} - 1]} = \left\{ e^{(H-h)\widehat{\rho}_2/E} - 1 + \frac{\widehat{\rho}_2}{\widehat{\rho}_1} [e^{h\widehat{\rho}_1/E} - 1] e^{(H-h)\widehat{\rho}_2/E} \right\}^{-1}. \quad (2.31)$$

The two kinematic conditions (2.20) and (2.21) and the continuity equations (2.12) can be combined to give the evolution equations

$$\frac{\partial}{\partial t} \int_0^h \phi dz + \frac{1}{r} \frac{\partial}{\partial r} r J_1 = 0, \quad \frac{\partial H}{\partial t} + \frac{1}{r} \frac{\partial}{\partial r} r (J_1 + J_2) = 0, \quad (2.32a,b)$$

where the fluxes of injected and ambient fluid are

$$J_1 = \int_0^h \phi u_f dz = - \int_0^h k \frac{\partial p}{\partial r} dz = -h \mathcal{K}_1 \left(\frac{\partial P}{\partial r} + \rho_2 \frac{\partial H}{\partial r} + \Delta \rho \frac{\partial h}{\partial r} \right), \quad (2.33a)$$

$$J_2 = \int_h^H \phi u_f dz = -M \int_h^H k \frac{\partial p}{\partial r} dz = -M(H - h) \mathcal{K}_2 \left(\frac{\partial P}{\partial r} + \rho_2 \frac{\partial H}{\partial r} \right), \quad (2.33b)$$

respectively, and where $\mathcal{K}_1 = h^{-1} \int_0^h k dz$ and $\mathcal{K}_2 = (H - h)^{-1} \int_h^H k dz$. The fluxes of injected and ambient fluid at the origin are

$$\lim_{r \rightarrow 0} (r J_1) = \frac{Q}{2\pi}, \quad \lim_{r \rightarrow 0} (r J_2) = 0. \quad (2.34a,b)$$

The gradient of the surface pressure P in (2.33) can be calculated by differentiation of the stress-balance condition (2.29), which eliminates \mathcal{P} from the model owing to the neglect of bending and tension in the overburden.

2.5. Brief summary of the model

The evolution of the upper surface at $z=H$ and the interface at $z=h$ between injected and ambient fluid are given by (2.32) and (2.33). In fact, the derivation of these equations applies for any general three-dimensional shallow geometry, in which case the coupled evolution equations can be summarized as

$$\frac{\partial H}{\partial t} - \nabla \cdot \left\{ [h\mathcal{K}_1 + M(H-h)\mathcal{K}_2] \left(\frac{E}{1-\Phi_0} \nabla \Phi + \rho_2 \nabla H \right) + h\mathcal{K}_1 \Delta \rho \nabla h \right\} = 0, \tag{2.35a}$$

$$\frac{\partial}{\partial t} \int_0^h \phi \, dz - \nabla \cdot \left\{ h\mathcal{K}_1 \left(\frac{E}{1-\Phi_0} \nabla \Phi + \rho_2 \nabla H + \Delta \rho \nabla h \right) \right\} = 0, \tag{2.35b}$$

where ∇ indicates the gradient operator in the plane normal to the direction of gravity, and the vertical integral of ϕ and the gradients of the surface porosity Φ can be calculated from (2.28) and (2.31), respectively.

The dimensionless parameters in (2.35) are the elastic modulus E , the viscosity ratio $M = \mu_1/\mu_2$, the scaled fluid densities ρ_1 and ρ_2 (or $\hat{\rho}_1 = (1 - \Phi_0)(1 - \rho_1)$ and $\hat{\rho}_2 = (1 - \Phi_0)(1 - \rho_2)$), and the initial porosity at the upper surface Φ_0 . The averages \mathcal{K}_1 and \mathcal{K}_2 are determined by specifying the permeability function $k(\phi)$.

Equations (2.35) provide a general formulation to describe shallow flow in a poro-elastic layer which cannot freely slip at its surfaces. They could be generalized to include, for example, a nonlinear constitutive law or a non-flat lower surface, or they can be reposed in the limit of no gravity (see (4.15)). For the remainder of this paper, we consider axisymmetric flow with a fixed constant flux Q of injection (in appendix A, we also consider the closely related problem of constant-pressure injections). We further focus on the geophysical context, for which the dimensionless stiffness E is relatively large. This transpires because the elastic moduli for rocks are typically appreciably larger than the lithostatic pressure difference across the layer. Rough parameter values from the sandstone formation at In Salah (Rutqvist *et al.* 2010), for example, suggest that $E \approx 1.3 \times 10^4$. In the asymptotic limit $E \rightarrow \infty$, the model reduces to the usual gravity-current equations in a rigid porous medium, as we will demonstrate in § 4.

From (2.28), flow-induced vertical variation in ϕ through the medium is relatively small when E is large. Thus, although a permeability function $k(\phi)$ is easily incorporated in the model via the vertical averages \mathcal{K}_1 and \mathcal{K}_2 in (2.33) and (2.35), the functional form of $k(\phi)$ has no significant effect on the dynamics. For the remainder of the paper we therefore make the simplifying assumption that k is constant, and set $k = \mathcal{K}_1 = \mathcal{K}_2 = 1$.

3. Results

We solved the coupled evolution equations (2.35) numerically in an axisymmetric domain of radial extent $r_{edge} \gg 1$, using a semi-implicit second-order finite-difference scheme, with constant-flux conditions in (2.34) and the initial conditions $H = 1$, $h = 0$, and $\phi = \phi_0$ given by (2.26). For this problem, one can show from a local analysis of the governing PDEs that the front of the injected fluid travels with a finite speed and spatial gradient (as for a classical gravity current in a non-deformable medium) while the uplift and its spatial gradient remain continuous there. As such, no special treatment was required in the numerical scheme to describe this moving front.

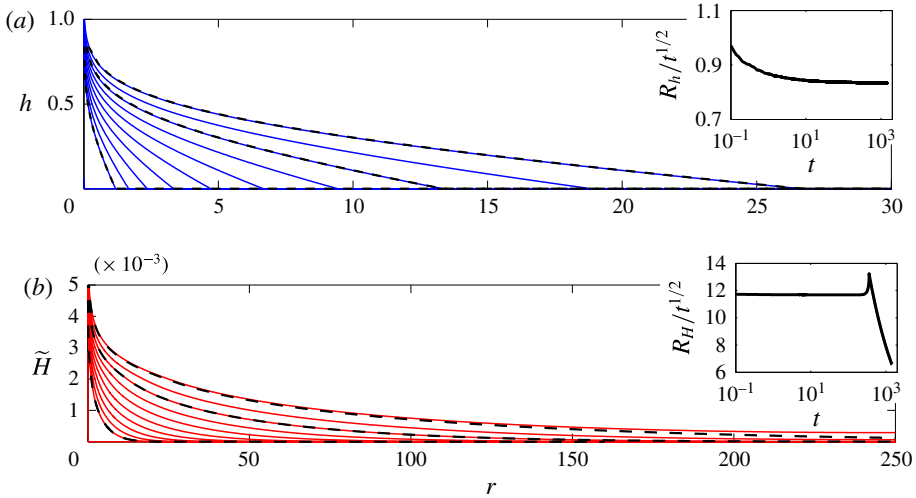


FIGURE 2. (Colour online) Snapshots from numerical simulations with the default parameter settings given at the start of § 3, with $r_{edge} = 250$, at times $t = 0, 2, 4, 8, 16, 32, 64, 128, 256, 512$ and 1024 (solid), together with the equivalent similarity solutions evaluated at $t = 2, t = 256$ and $t = 1024$ (dashed). (a) The height $h(r, t)$ of the injected current and (b) the uplift $\tilde{H}(r, t) = H(r, t) - 1$. Note the different horizontal scales. The insets show the radial extents R_h and R_H of the injected current and the uplift, respectively, defined as $h(R_h, t) = 0$ and $\tilde{H}(R_H, t) = 10^{-5}$.

In the case of an unbounded domain, the system of equations and boundary conditions (2.34) and (2.35) with a constant flux of injection contains no natural radial length scale and so permits a self-similar solution in terms of the variable $\eta \equiv r/t^{1/2}$. In § 3.1, we show that solutions converge to this self-similar form, and subsequently demonstrate the dependence of the similarity solutions on the different parameters of the model. Unless otherwise stated, we use default parameter settings of $E = 16, Q = 0.1, \rho_2 = 0.5, \rho_1 = 0.7$ and $\Phi_0 = 0.3$.

3.1. Convergence to self-similar form

Figure 2 shows snapshots of the height h of the interface and of the surface displacement $\tilde{H} = H - 1$. Comparison of these snapshots reveals that h and H have quite different profiles. In particular, the uplift of the medium spreads far ahead of the location of the injected fluid. As remarked above, the injected current has a sharp front at $r = R_h(t)$, where $h \rightarrow 0$ with finite slope, with no discernible signature in the profile of the upper surface at that point. By contrast, the upper surface smoothly levels off with no clear nose; that is, it does not have compact support. Indeed, we will show in § 4.1 that the uplift propagates in a linear diffusive manner ahead of the injected current. To measure the radial extent of the uplift, $R_H(t)$, we are therefore forced to adopt a nominal threshold amplitude; in figure 2 this is chosen to be 10^{-5} , so that $H(R_H, t) = 10^{-5}$.

Figure 2 also demonstrates that solutions evolve to self-similar form, with both $h(r, t)$ and $\tilde{H}(r, t)$ converging to specific functions of the similarity variable $\eta \equiv r/t^{1/2}$. The insets in figure 2 show in more detail how the front of the injection spreads self-similarly after a short transient, whereas the (thresholded) radial extent of the

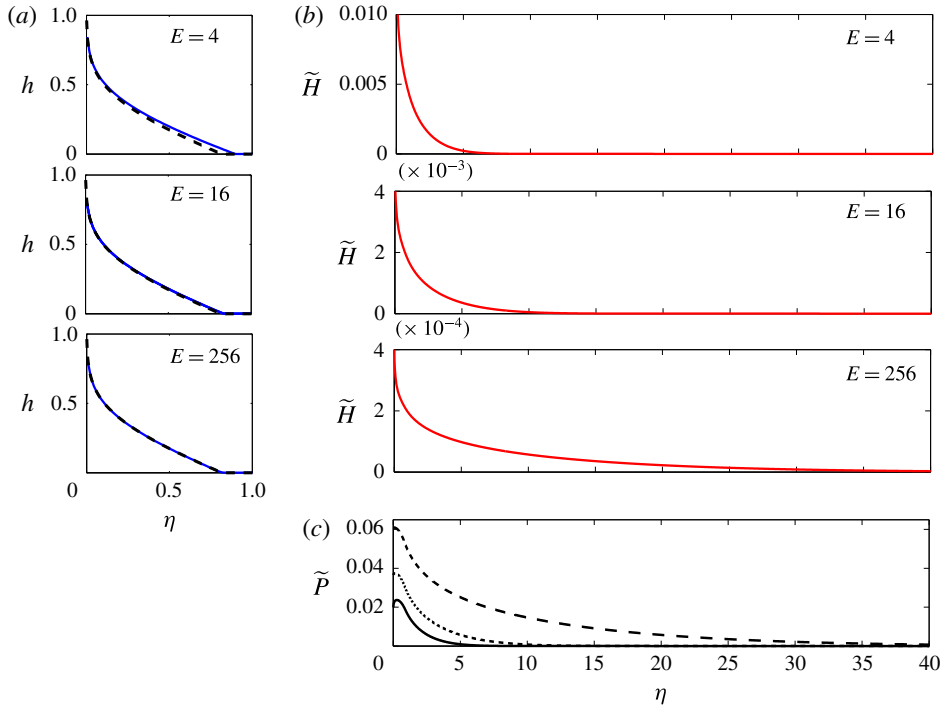


FIGURE 3. (Colour online) Similarity solutions with $M = 1$ for different values of the elastic modulus E as marked, in terms of the similarity variable $\eta \equiv r/t^{1/2}$. (a) The height $z = h$ of the injected current (solid) with the similarity solution for $E \rightarrow \infty$ (dashed; see § 4.2). (b) The uplift $\tilde{H} = H - 1$. (c) The increase in the surface pore pressure $\tilde{P} = P - \mathcal{P}$, for $E = 4$ (solid), $E = 16$ (dotted) and $E = 256$ (dashed). Note the different scales in the different horizontal scales between (a) and (b), and the different vertical scales in (b).

uplift adopts the self-similar form immediately, but deviates from this scaling once $R_H(t)$ reaches the far edge of the domain. Inevitably, this collision leads to a slight deviation from the self-similar form for the profiles of \tilde{H} in the vicinity of the edge of the domain at later times (see comparison of dashed and solid lines in figure 2b). However, the self-similar form of $h(r, t)$ and $\tilde{H}(r, t)$ is still maintained over the bulk of the domain.

3.2. Similarity solutions with $M = 1$

The similarity solutions can be obtained directly by rewriting the governing PDEs (2.35) as a fourth-order system of ODEs, using the transformations $\partial/\partial r \rightarrow \partial/\partial \eta$ and $\partial/\partial t \rightarrow (-\eta/2)\partial/\partial \eta$. Alternatively, provided they have converged to self-similar form, similarity solutions can be extracted directly from suitable snapshots of solutions of the PDEs. Here we predominantly use the latter approach, but have verified that it gives the same answer as the former.

Figure 3 shows solutions of the interface height h , the uplift $\tilde{H} = H - 1$, and the increase in the pore pressure at the upper surface, $\tilde{P} = P - \mathcal{P}$, for different values of the elastic modulus E . The figure confirms the previous observation that the uplift spreads ahead of the position of the injected fluid, but also shows that

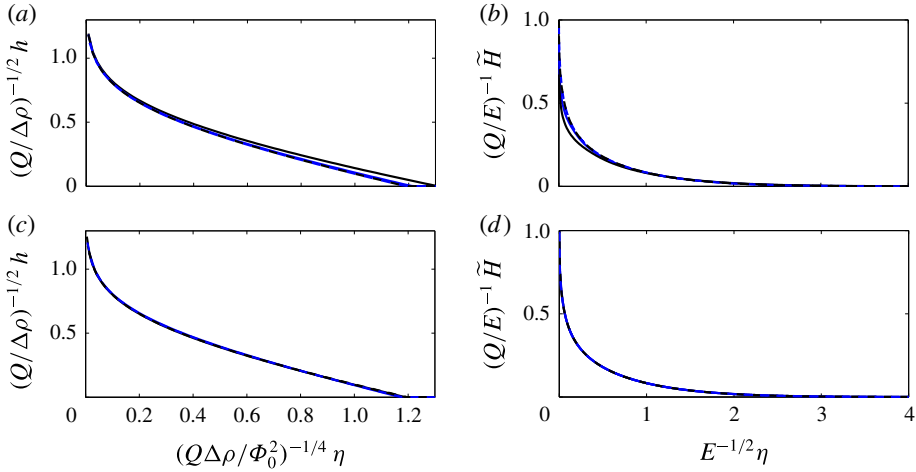


FIGURE 4. (Colour online) Similarity solutions of (a,c) the scaled interface height and (b,d) the scaled uplift against the scaled similarity variable. (a,b) Comparison for different values of the elastic modulus E : $E = 4$ (black solid), $E = 16$ (blue solid), $E = 256$ (black dashed), $E = 1024$ (blue dashed). (c,d) Comparison for $E = 256$ and different values of the other parameters: $Q = 0.1$, $\rho_1 = 0.7$, $\Phi_0 = 0.3$ (black solid), $Q = 0.025$ (blue solid), $\rho_1 = 0.9$ (black dashed), $\Phi_0 = 0.1$ (blue dashed). All unquoted parameters are given by the default values at the start of § 3. The only appreciable deviation from the scalings is for $E = 4$ in (a,b).

h and H have a quite different dependence on E . In particular, while h is largely unaffected by changes in E (figure 3a), the radial spread of the uplift increases and its magnitude decreases as the medium becomes stiffer (figure 3b). Profiles of the surface overpressure \tilde{P} , which is a potentially important variable when considering the possibility of fractures or failures in the medium, mirror those of the uplift (figure 3c), except near the point in injection where the pressure profiles are rounded off. Unlike the uplift, the magnitude of \tilde{P} increases with the stiffness of the medium.

Figure 4 shows solutions of h and \tilde{H} for a selection of different parameter values. The results collapse onto roughly the same profiles when the similarity variable $\eta \equiv r/t^{1/2}$ and h are scaled by

$$\eta \sim \left(\frac{Q\Delta\rho}{\Phi_0^2}\right)^{1/4}, \quad h \sim \left(\frac{Q}{\Delta\rho}\right)^{1/2}, \tag{3.1a,b}$$

(figure 4a,c) and when η and \tilde{H} are scaled by

$$\eta \sim E^{1/2}, \quad \tilde{H} \sim \frac{Q}{E}, \tag{3.2a,b}$$

(figure 4b,d). A theoretical basis for these scalings will be discussed in § 4.

3.3. Similarity solutions with viscosity ratio $M \neq 1$

There are a number of differences to the dynamics discussed above when $M = \mu_1/\mu_2 \neq 1$. Figure 5 shows that, for $M < 1$ (ambient fluid is more viscous than

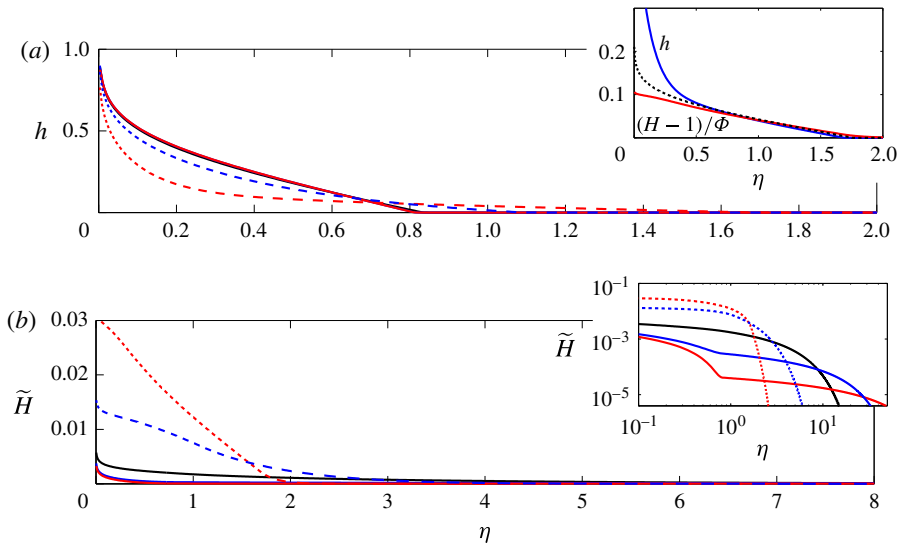


FIGURE 5. (Colour online) Similarity solutions for different values of the viscosity ratio $M = \mu_1/\mu_2$: $M = 0.01$ (red dashed), $M = 0.1$ (blue dashed), $M = 1$ (black solid), $M = 10$ (blue solid) and $M = 100$ (red solid). (a) The height h , with (inset) a comparison for $M = 0.01$ with the asymptotic results of § 4.3, showing h (blue), $(H - 1)/\Phi_0$ (red) and the solution (black dashed) of the relevant asymptotic evolution equation (4.19b). (b) The uplift \tilde{H} , with (inset) the same data on logarithmic axes. Note that, in (a), the profiles for $M \geq 1$ are very similar and the separate lines are difficult to distinguish.

injected fluid), both the height of the injected current and the height of the uplift differ significantly from when $M = 1$. The injected current extends further but the height is lower, as has been observed in non-deformable porous layers (Nordbotten & Celia 2006; Pegler, Huppert & Neufeld 2014), while the magnitude of the uplift increases. The uplift also becomes more localized to the position of the injected fluid rather than spreading ahead of the current. For $M > 1$ (figure 5) (ambient fluid is less viscous than injected fluid), the height of the injected current is almost indistinguishable from when $M = 1$, although the uplift is enhanced and is more localized when M is increased (figure 5b; inset). The different behaviour of the system for $M \neq 1$ is rationalized by the asymptotic analysis of the model in the following section. We find that the behaviour for $M > 1$ can be explained within the framework of an analysis for general M (§§ 4.1 and 4.2), but a quite distinct set of scalings for both the uplift and the current emerge in the limit $M \ll E^{-1/2}$, as discussed in § 4.3. As for a non-deformable medium (see Pegler *et al.* 2014), this axisymmetric, shallow-layer formulation does not predict Saffman–Taylor fingering for any values of M .

4. Asymptotic limits of the model for large elastic modulus $E \gg 1$

The numerical solutions indicate that both the uplift and the injected current converge to the same self-similar form in terms of $\eta \equiv r/t^{1/2}$. However, both the form of the profiles of h and H and their dependence on the different parameters of the model are quite different. In particular, the uplift propagates far ahead of the injected current, which appears to be almost independent of E for $E > O(10)$. In this section

we rationalize the different features of the injected current and the uplift by means of an asymptotic analysis of the model for $E \gg 1$. We find that the uplift has a radial scale $\sim E^{1/2}$ and obeys a linear diffusion equation ahead of the injected fluid (§ 4.1), which itself has an $O(1)$ radial extent and a form that reduces to the standard solution for a gravity current in a non-deformable medium (§ 4.2). Interestingly, the separation of radial scales between uplift and injected fluid breaks down if the injected fluid is much less viscous than the ambient fluid, such that $M \ll E^{-1/2} \ll 1$; a new set of scalings emerge in this limit, and both h and H have a radial scale $\sim E^{1/4}$ (§ 4.3).

4.1. *The uplift*

Ahead of the injected current, $h = 0$ and the hydrostatic pressure and porosity profiles, given from (2.27) and (2.28), are

$$p = P + \rho_2(H - z), \tag{4.1}$$

$$\phi = 1 - (1 - \Phi)e^{(H-z)\hat{\rho}_2/E}; \quad \Phi = 1 - (1 - \Phi_0)\frac{e^{\hat{\rho}_2/E} - 1}{e^{H\hat{\rho}_2/E} - 1}, \tag{4.2a,b}$$

respectively. The evolution equation for the uplift H , given from (2.32), is

$$\frac{\partial H}{\partial t} = \frac{M}{r} \frac{\partial}{\partial r} \left\{ rH \left[\rho_2 + \frac{\hat{\rho}_2(1 - \Phi_0)[e^{\hat{\rho}_2/E} - 1]}{[e^{H\hat{\rho}_2/E} - 1]^2} e^{H\hat{\rho}_2/E} \right] \frac{\partial H}{\partial r} \right\}. \tag{4.3}$$

Note that (4.3) is also recovered throughout the domain in the case when the injected fluid is identical to the ambient fluid ($\rho_1 = \rho_2$ and $\mu_1 = \mu_2$).

For $E \gg 1$, (4.3) reduces to

$$\frac{\partial H}{\partial t} = \frac{1}{r} \frac{\partial}{\partial r} \left[\frac{MEr}{H} \frac{\partial H}{\partial r} \right] = \frac{1}{\tilde{r}} \frac{\partial}{\partial \tilde{r}} \left[\frac{\tilde{r}}{H} \frac{\partial H}{\partial \tilde{r}} \right], \tag{4.4}$$

in terms of a rescaled radial coordinate $\tilde{r} = r/(ME)^{1/2}$. This rescaling quantifies the observed scale separation in the numerical solutions: the uplift extends a distance $\sim (ME)^{1/2}$ ahead of the injected current. On the relatively long radial scale \tilde{r} , the injection appears as a point source of ambient fluid with flux

$$\lim_{\tilde{r} \rightarrow 0} \left[ME \frac{\tilde{r}}{H} \frac{\partial H}{\partial \tilde{r}} \right] = -\frac{Q}{2\pi}. \tag{4.5}$$

The source therefore drives a weak uplift $H = 1 + \tilde{H}$, with $\tilde{H} = O(Q/(ME)) \ll 1$ satisfying the linear diffusion equation

$$\frac{\partial \tilde{H}}{\partial t} = \frac{1}{\tilde{r}} \frac{\partial}{\partial \tilde{r}} \left(\tilde{r} \frac{\partial \tilde{H}}{\partial \tilde{r}} \right), \tag{4.6}$$

from (4.4), which rationalizes the diffusive character of the numerical solutions. Moreover, the self-similar form of the far-field uplift is given from (4.5) and (4.6) by

$$H - 1 = \frac{Q}{ME} f \left(\frac{\eta}{\sqrt{ME}} \right), \tag{4.7}$$

where $f(x)$ satisfies the ODE $(xf')' + x^2f'/2 = 0$. The predictions in (4.7) confirm the observed scalings shown in figure 4 and reported in (3.2), and generalize them for $M \neq 1$ and $M \gg E^{-1/2}$ (see § 4.3). The separation of length scales between the injected current and the uplift implies that the latter is insensitive to the detailed dynamics of the injected fluid in this limit. Note that the scaling in (4.7b) is just the classical poro-elastic diffusion scale; see e.g. Coussy (2004).

4.2. The injected current

For $E \gg 1$ and $h > 0$, the porosity becomes

$$\phi = \Phi = 1 - \frac{1 - \Phi_0}{H}, \tag{4.8}$$

to leading order, from (2.28) and (2.31), such that ϕ is independent of depth. Hence

$$\frac{\partial \Phi}{\partial H} = \frac{1 - \Phi_0}{H^2}, \quad \frac{\partial \Phi}{\partial h} = -\frac{h(1 - \Phi_0)^2 \Delta \rho}{EH^2}, \tag{4.9a,b}$$

which can be used to evaluate $\partial P/\partial r$ and thus the leading-order fluxes J_1 and J_2 in (2.33):

$$J_1 = -\frac{Eh}{H^2} \frac{\partial H}{\partial r} - \Delta \rho \left[h - \frac{(1 - \Phi_0)h^2}{H^2} \right] \frac{\partial h}{\partial r}, \tag{4.10a}$$

$$J_2 = -\frac{EM(H-h)}{H^2} \frac{\partial H}{\partial r} + \frac{M\Delta \rho(1 - \Phi_0)h(H-h)}{H^2} \frac{\partial h}{\partial r}. \tag{4.10b}$$

In order to achieve a balance in the evolution equations (2.32), J_1 and J_2 must be $O(1)$, which implies that $\partial H/\partial r = O(E^{-1})$ in (4.10). Hence, as above, $H = 1 + \tilde{H}$ with $\tilde{H} = O(E^{-1}) \ll 1$, and so

$$\frac{\partial H}{\partial t} = -\frac{1}{r} \frac{\partial}{\partial r} r(J_1 + J_2) = O(E^{-1}) \ll 1, \tag{4.11}$$

which indicates that the total flux $r(J_1 + J_2)$ is a constant to leading order, given by $Q/2\pi$. The slope of the uplift becomes

$$E \frac{\partial \tilde{H}}{\partial r} = -\Delta \rho \left[\frac{1}{[h + (1-h)M]} - (1 - \Phi_0) \right] h \frac{\partial h}{\partial r} - \frac{Q}{2\pi r[h + (1-h)M]}, \tag{4.12}$$

to leading order, from (4.11) and (4.10). The terms involving the uplift can thus be eliminated from (4.10a), and the evolution equation (2.32a) reduces to

$$\Phi_0 \frac{\partial h}{\partial t} = \frac{1}{r} \frac{\partial}{\partial r} \left[\frac{-Qh}{2\pi[h + (1-h)M]} + \Delta \rho \frac{rh(1-h)M}{h + (1-h)M} \frac{\partial h}{\partial r} \right] + O(E^{-1}), \tag{4.13}$$

which is the standard evolution equation for the height of a gravity current with a fixed flux Q in a confined, non-deformable, porous medium (see, e.g. Pegler *et al.* 2014). Provided that the injected current does not fill the layer, (4.13) can be approximated by taking the limit $h \ll 1$ to give the equation for a gravity current in an unbounded medium (Lyle *et al.* 2005), which yields similarity scalings of

$$h \sim \left(\frac{Q}{\Delta \rho} \right)^{1/2}, \quad \eta \equiv r/t^{1/2} \sim \left(\frac{Q\Delta \rho}{\Phi_0^2} \right)^{1/4}, \tag{4.14a,b}$$

for the height and extent of the injected current. These scalings were observed in the full similarity solutions in (3.1) and in figure 4. Interestingly, the scalings appear to hold all the way down to $E = 4$, which suggests that the influence of the uplift on the injected current is negligible except in very deformable media (small E).

A further interesting feature of the leading-order equations (4.8)–(4.10) is that they correspond to the limit of neglecting gravity (i.e. purely pressure-driven flow), because $E \propto 1/g$ (cf. (2.15)). However, in this limit we cannot deduce that H is constant to leading order, as in (4.11), since time has also been scaled by $1/g$ (see § 2.2). Instead, the time derivatives in the evolution equations must be balanced with terms proportional to E in (4.10) to give equations for the evolution of h and H in the absence of gravity:

$$\frac{\partial}{\partial \tilde{t}}(\Phi h) = \frac{1}{r} \frac{\partial}{\partial r} \left[\frac{rh}{H^2} \frac{\partial H}{\partial r} \right]; \quad \frac{\partial H}{\partial \tilde{t}} = \frac{1}{r} \frac{\partial}{\partial r} \left[\frac{r[h + (H - h)M]}{H^2} \frac{\partial H}{\partial r} \right], \tag{4.15a,b}$$

where $\tilde{t} = Et$ and $\Phi = 1 - (1 - \Phi_0)/H$ from (4.8). The evolution of both injected fluid and uplift are governed by gradients in the slope of the overburden in this limit.

4.3. Small viscosity ratio $M \equiv \mu_1/\mu_2 \ll 1$

The features of the model for $E \gg 1$ discussed above change when the viscosity ratio M is sufficiently small, such that the ambient fluid is much more viscous than the injected fluid. This is potentially the case for CO₂ sequestration, where the injected CO₂ has a much lower viscosity than the ambient brine; we consider this issue in § 6.

The key to understanding the change in behaviour is first to observe that the flux of ambient fluid, J_2 , is proportional to M , and so the evolution equations (2.32) can be combined to give

$$\frac{\partial}{\partial t}(\Phi h) = \frac{\partial H}{\partial t} - O(M), \tag{4.16}$$

since the porosity is still given by (4.8) for $E \gg 1$ and so is independent of depth. Equation (4.16) implies

$$h = \frac{\tilde{H}}{\Phi} + O(M). \tag{4.17}$$

In other words, the height of the injected current is small, and it undercuts the more viscous ambient fluid which is plugging up the porous layer. Moreover, the uplift becomes coupled directly to the injected fluid current and no longer diffuses ahead.

In view of (4.17), the leading-order fluxes J_1 and J_2 in (4.10) simplify still further and the evolution equations (2.32) reduce to

$$\frac{\partial}{\partial \tilde{t}}(\Phi h) = \frac{E}{r} \frac{\partial}{\partial r} \left(\frac{rh}{H^2} \frac{\partial \tilde{H}}{\partial r} \right), \quad \frac{\partial \tilde{H}}{\partial \tilde{t}} = \frac{E}{r} \frac{\partial}{\partial r} \left[\frac{r[h + (H - h)M]}{H^2} \frac{\partial \tilde{H}}{\partial r} \right]. \tag{4.18a,b}$$

To satisfy both (4.17) and (4.18) simultaneously, we can no longer deduce that $\tilde{H} = O(E^{-1})$ as in § 4.2. Instead, provided $M \ll h \ll 1$ (which we establish below), we find that (4.17) and (4.18) reduce to

$$h = \frac{H - 1}{\Phi}; \quad \frac{\partial h}{\partial \tilde{t}} = \frac{E}{r} \frac{\partial}{\partial r} \left(rh \frac{\partial h}{\partial r} \right), \tag{4.19a,b}$$

and a change in the scaling of the radial structure of the solution is required. In particular, (4.19) (which has the same form as a standard equation for a gravity current in a porous medium) together with the boundary condition $-Q/2\pi = \Phi_0 Erh(\partial h/\partial r)$ as $r \rightarrow 0$, furnish the similarity solution,

$$h = \frac{H-1}{\Phi_0} = \left(\frac{Q}{\Phi_0 E}\right)^{1/2} f\left(\frac{\eta}{(QE/\Phi_0)^{1/4}}\right), \quad (4.20)$$

where $f(x)$ satisfies the ODE $(xff')' + x^2f/2 = 0$. Thus, the height of the current and uplift are indeed small: $h \sim \tilde{H} \sim O(E^{-1/2})$. The condition $M \ll h$ demands that $M \ll E^{-1/2} \ll 1$, which identifies the viscosity ratio for which the scalings change. If either $M > O(E^{-1/2})$ or $h \ll M$, then (4.18b) reduces to the linear diffusion equation (4.6) discussed in § 4.1, and the uplift again diffuses ahead of the current.

The scalings in (4.20) can be compared with the previously identified scalings in (4.7) and (4.14). There is a transition from the injected current being driven by buoyancy forces and evolving independently of E for $M = O(1)$, scaling as in (4.14), to the current being independent of buoyancy and being controlled by E as $M \rightarrow 0$, with scaling (4.20a,b). The magnitude of the uplift also becomes independent of M to leading order. These asymptotic results are consistent with the trends in the numerical results of figure 5; in particular, figure 5(a; inset) shows a relatively good agreement between direct measurement of h and the predictions of h using either (4.19a) or solutions to (4.19b).

5. Laboratory experiments

5.1. Experimental results

To complement the theory, we carried out laboratory experiments using polyacrylamide hydrogel particles. Dry particles swell to roughly 40 times their size on the addition of water, and form soft, elastic, roughly spherical beads of radius 0.38 ± 0.08 mm. We filled the base of a cylindrical tank, of radius of 445 mm, to a depth of $H_0 = 35$ mm with a layer of hydrogel particles to form a deformable porous medium (figure 6a). Because the particles consist predominantly of water, their density is only very slightly higher than 1 g cm^{-3} . The saturated bed of particles was overlain by a flexible but impermeable polydimethylsiloxane (PDMS) sheet of thickness 5 mm. The sheet fitted closely inside the tank, such that water did not leak around the edges during an experiment. There was a small hole at the base in the centre of the tank through which water could be injected at a fixed flux (using a peristaltic pump) or allowed to drain. Interstitial air in the medium was removed by first significantly over-saturating the particles to produce a thin slurry, before slowly draining excess water to produce a medium that was fully saturated.

The experiments were intended to provide a relatively simple qualitative comparison with the theoretical model in the limit that the injected and ambient fluid are identical. One-dimensional compression tests suggested that the saturated medium had an elastic modulus of $K + 4G/3 \approx 20\text{--}30$ kPa, in rough agreement with previously quoted values for this material (MacMinn *et al.* 2015). The dimensionless stiffness therefore lay in the range $70 \lesssim E \lesssim 80$, and so was fairly large, as in the limit considered in our analysis. Despite this, there are a number of complications associated with this experimental set-up which render a systematic comparison with the theoretical model difficult (see § 5.2).

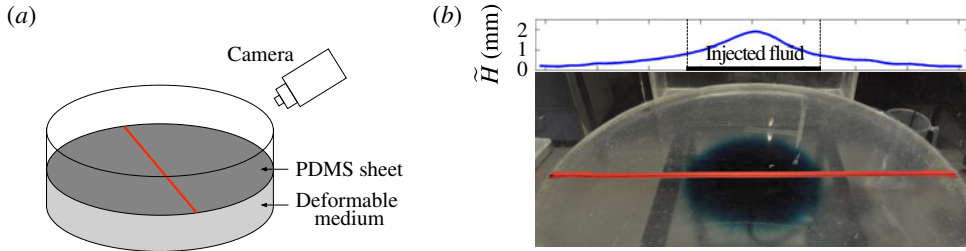


FIGURE 6. (Colour online) (a) A schematic of the experimental set-up. (b) An image from an experiment in which the injected water was dyed blue to distinguish it from the clear ambient water. The profile above shows the uplift of the upper surface, as measured by the deflection of the line on the PDMS sheet, and demonstrates that the uplift travels ahead of the blue fluid. The flux was $Q = 100 \text{ cm}^3 \text{ min}^{-1}$ and the image was taken roughly 2 min after the start of injection.

The main variable that was changed between experiments was the injection rate. We also carried out sets of experiments for different depths H_0 of the medium, which are not presented but exhibited qualitatively similar results to those discussed here. During each experiment, we took measurements of the uplift by using a camera to track a line drawn on the surface of the PDMS sheet. The camera was located 770 mm from the centre of sheet at an angle of 35° from the horizontal. Figure 6(b) shows a picture from an experiment in which the injected fluid was dyed blue, together with the measured profile of the uplift of the upper surface. Note that the injected fluid noticeably lags behind the measured uplift.

Figure 7 shows measurements of the height of the upper surface over time, for two different injection rates Q . The uplift is qualitatively similar to the numerical solutions (see, for example, figure 3b), except near to the point of injection, where the profiles are smoother. This difference is most likely due to bending stresses in the PDMS sheet, which we estimate to be important on length scales of a few centimetres (see § 5.2). Such stresses eliminate the logarithmic divergence of the uplift \tilde{H} for $r \rightarrow 0$ predicted by the model (see appendix A) by rounding off the profile there.

Comparison of figure 7(a,b) suggests that the main difference between the measurements at different injection rates is the magnitude of the uplift, and that the rate at which the uplift propagates radially is largely independent of the flux. This observation is corroborated by snapshots of the uplift for a range of different values of the flux (figure 8), which shows that the profiles collapse onto roughly the same curve when scaled by the injection rate Q , in agreement with the theoretical prediction in (4.7a).

Given that the uplift scales with the injection rate, we identify the radial extent of the uplift by choosing a threshold in \tilde{H}/Q . More specifically, we define

$$R_H = \min \{r : \tilde{H} < 2Q \times 10^{-3}\}. \quad (5.1)$$

Measurements of R_H from the experiments (figure 9) agree qualitatively with the predicted scalings in (4.7), with the radial spread being largely independent of the injection rate Q and scaling with $t^{1/2}$ until R_H reaches the edge of the tank. The spread also slightly accelerates close to the boundary of the tank, as observed in the numerical solutions in a finite domain (figure 2b inset). Contrary to theory, the uplift

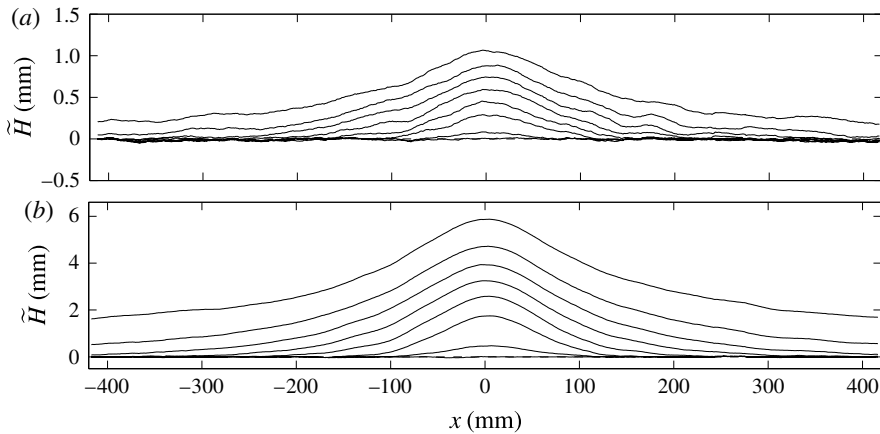


FIGURE 7. Experimental measurements of the height \tilde{H} of the deviation of the upper surface, in mm, at times $t = 2, 4, 8, 16, 32, 64, 128$ and 256 s. (a) Injection rate $Q = 25 \text{ cm}^3 \text{ min}^{-1}$. (b) $Q = 200 \text{ cm}^3 \text{ min}^{-1}$. The coordinate x measures the radial distance from the point of injection, such that $r = |x|$.

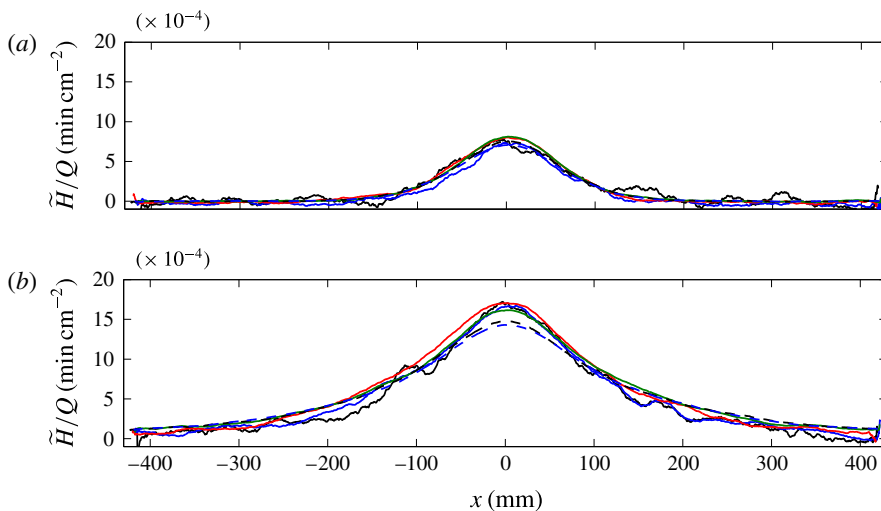


FIGURE 8. (Colour online) Experimental measurements of the height \tilde{H} of the deviation of the top surface scaled by the injection rate Q , at times (a) $t = 10$ s and (b) $t = 100$ s, for different injection rates $Q = 25 \text{ cm}^3 \text{ min}^{-1}$ (black solid), $Q = 50 \text{ cm}^3 \text{ min}^{-1}$ (blue solid), $Q = 100 \text{ cm}^3 \text{ min}^{-1}$ (red solid), $Q = 200 \text{ cm}^3 \text{ min}^{-1}$ (green solid), $Q = 300 \text{ cm}^3 \text{ min}^{-1}$ (black dashed) and $Q = 400 \text{ cm}^3 \text{ min}^{-1}$ (blue dashed). The noise in the profiles with the lowest injection rates reflects the sub-pixel resolution of the processed images (achieved using a Gaussian fit to the intensity of the tracked line), which was roughly $50 \text{ }\mu\text{m}$.

spreads initially (up to ~ 10 s) more rapidly than $t^{1/2}$ and the height above the point of injection increases steadily. The disagreement with theory is again most likely due to bending stresses in the overburden near the origin, at least at early times. At

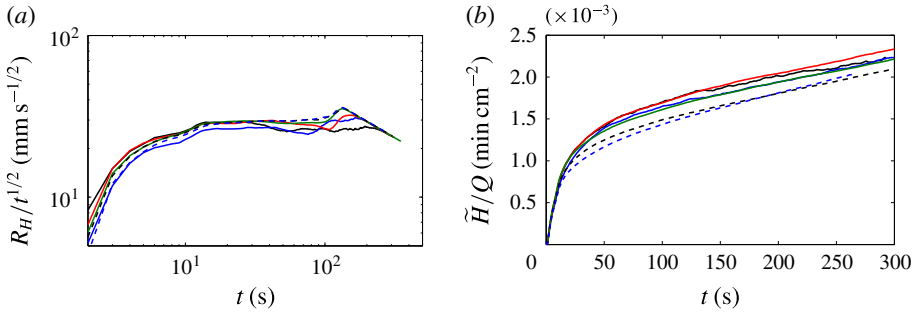


FIGURE 9. (Colour online) Experimental measurements for different injection rates: $Q = 25 \text{ cm}^3 \text{ min}^{-1}$ (black solid), $Q = 50 \text{ cm}^3 \text{ min}^{-1}$ (blue solid), $Q = 100 \text{ cm}^3 \text{ min}^{-1}$ (red solid), $Q = 200 \text{ cm}^3 \text{ min}^{-1}$ (green solid), $Q = 300 \text{ cm}^3 \text{ min}^{-1}$ (black dashed) and $Q = 400 \text{ cm}^3 \text{ min}^{-1}$ (blue dashed). (a) The radial extent R_H , defined by (5.1), of the uplift, scaled by $t^{1/2}$. The measurements are approximately independent of Q and show a scaling of $t^{1/2}$ until R_H reaches the edge of the tank. (b) The height $\tilde{H}(r=0)$ above the point of injection, scaled by Q .

later times, the pressure signal has reached the edge of the domain and the entire overburden is lifting up.

5.2. Limitations of the experiments

The experimental system provides a simple laboratory-scale deformable porous medium, with which we have been able to confirm qualitatively some of the theoretical results. There are some difficulties in using hydrogel particles as an idealized poro-elastic medium, which prevented a more quantitative comparison with the model. In particular, the particles are always coated with a layer of water, and it is not clear whether their aqueous contents continually leak out. In this situation it is very difficult to distinguish the effective solid phase from the fluid, and therefore to measure the initial porosity. We also found that the elastic modulus of the saturated medium varies appreciably with the porosity, which complicates the characterization of the properties of the medium.

One of the notable features of the experimental results is the influence of bending in the overburden around the point of injection. The flexural rigidity B of the PDMS sheet was $B \approx 0.024 \text{ Pa m}^3$ (given a Young's modulus of $\approx 1.8 \text{ MPa}$, a thickness of 5 mm and a Poisson ratio of 0.45 ; see Lister, Peng & Neufeld, 2013). The relative importance of bending in the balance of stresses (2.23) at the upper surface is given by the ratio of the bending pressure $B\nabla^4 H$ to the hydrostatic pressure $\rho g H$. Such a balance gives a rough length scale of $r \approx 4 \text{ cm}$ over which bending is likely to affect the uplift, which is consistent with the length scale of the rounding of the profiles around the point of injection in figures 7 and 8. A similar analysis can be carried out in a geophysical context: for an overburden rock with Young's modulus 10 GPa and depth 1 km , bending of the overburden would affect the uplift for roughly 1 km around the injection site.

6. Conclusions

In this paper, we used a two-phase poro-elastic formulation and shallow-layer scalings to describe the injection and gravity-driven spread of fluid in an axisymmetric

| Regime | h | $\eta \equiv r/t^{1/2}$ | $H - H_0$ | $\eta \equiv r/t^{1/2}$ |
|---|---|---|---|---|
| $\left(\frac{\mu_1}{\mu_2}\right)^2 \gtrsim \left(\frac{\tilde{E}}{\rho_s g H_0}\right)^{-1} \ll 1$ | $\left[\frac{Q\mu_1}{gk_0(\rho_1 - \rho_2)}\right]^{1/2}$ | $\left[\frac{Q(\rho_1 - \rho_2)gk_0}{\mu_1\Phi_0^2}\right]^{1/4}$ | $\frac{QH_0\mu_2}{k_0\tilde{E}}$ | $\left[\frac{k_0\tilde{E}}{\mu_2}\right]^{1/2}$ |
| $\left(\frac{\mu_1}{\mu_2}\right)^2 \ll \left(\frac{\tilde{E}}{\rho_s g H_0}\right)^{-1} \ll 1$ | $\left[\frac{QH_0\mu_1}{k_0\tilde{E}\Phi_0}\right]^{1/2}$ | $\left[\frac{Qk_0\tilde{E}}{\mu_1\Phi_0H_0}\right]^{1/4}$ | $\left[\frac{QH_0\mu_1\Phi_0}{k_0\tilde{E}}\right]^{1/2}$ | $\left[\frac{Qk_0\tilde{E}}{\mu_1\Phi_0H_0}\right]^{1/4}$ |

TABLE 1. A summary of the dimensional scalings of the heights $z = h$ and $z = H$ and of the corresponding similarity variables $\eta \equiv r/t^{1/2}$ for injection with a constant (dimensional) flux Q , where H_0 is the depth of the layer, g is the gravitational acceleration, ρ_1 , ρ_2 and ρ_s are the densities of the injected and ambient fluids and of the solid phase, μ_1 and μ_2 are the viscosities of the injected and ambient fluids, Φ_0 and k_0 are characteristic porosity and permeability scales (all respectively), and $\tilde{E} \equiv K + 4G/3$ combines the bulk modulus K and shear modulus G of the porous medium. Note that the scalings presented for h and η in the top line are the scalings for a porous gravity current in a deep domain (Lyle *et al.* 2005), which will apply for as long as the injection does not fill up the porous layer; see Pegler *et al.* (2014). The scaling of η for the uplift in the top line is the classical poro-elastic diffusion scale (Coussy 2004).

poro-elastic layer lying on a rigid horizontal substrate and below a flexible overburden. We derived a model coupling the evolution of the height $h(r, t)$ of the injected current with the resultant deformation of the medium and corresponding uplift $H(r, t)$ of the overburden. In the absence of an external radial length scale, both h and H are described by self-similar solutions with respect to the similarity variable $\eta \equiv r/t^{1/2}$. In geophysical settings, the dimensionless modulus or stiffness E , which is the ratio of elastic to gravitational stresses, is typically large, and we focused on that limit in this work.

We found that deformation of the medium has, in general, only a very small effect on the dynamics of the injected fluid. In many geological cases, the current evolves as a standard gravity current in a rigid porous medium (see the scalings in table 1), and is largely independent of the stiffness for moderate to large E , provided the viscosity of the ambient fluid μ_2 is not much larger than that of the injected fluid μ_1 (specifically, $\mu_1/\mu_2 > O(E^{-1/2})$). The uplift of the medium, on the other hand, varies significantly with the stiffness. There is a separation of radial scales between the uplift and the injected fluid: the uplift spreads in a linear diffusive manner ahead of the injected fluid and is insensitive to the detailed dynamics of the spreading current (see table 1).

Owing to this diffusive character, there is no true front to the outgoing signal of the uplift. Instead, its radial spread $r_H(\mathcal{H})$ must be defined using a prescribed threshold $H - H_0 = \mathcal{H}$ in the elevation change. In fact, because the full diffusion solution of (4.7) has a Gaussian nose, it can be shown that

$$r_H \sim \left(\frac{k_0\tilde{E}}{\mu_2}\right)^{1/2} \left[\log\left(\frac{Q\mu_2}{\mathcal{H}k_0\tilde{E}}\right)\right]^{1/2} t^{1/2}, \tag{6.1}$$

where the dependence on viscosity μ_2 , elastic modulus $\tilde{E} \equiv (K + 4G/3)$, injection rate Q and permeability scale k_0 follow from the detailed similarity solution of (4.7).

The radial extent r_H of the uplift is therefore only weakly dependent on the rate of injection Q , and is independent of the buoyancy terms, the initial porosity Φ_0 , and the viscosity of injected fluid μ_1 , all of which affect the evolution of the injected current.

Both the uplift and the height of the injected fluid are functions of the same similarity variable, and the ratio r_h/r_H of the radial spread of injected fluid to that of the uplift is therefore independent of time. Using (6.1) and the scalings in table 1, we estimate

$$\frac{r_h}{r_H} \sim \left[\frac{Q(\rho_1 - \rho_2)g\mu_2^2}{k_0\tilde{E}^2\Phi_0^2\mu_1} \right]^{1/4} \left[\log \left(\frac{Q\mu_2}{\mathcal{H}k_0\tilde{E}} \right) \right]^{-1/2}. \quad (6.2)$$

If an uplift of \mathcal{H} is observed at a radial distance $r_{\mathcal{H}}$, this ratio allows one to determine the predicted extent r_h of the injected fluid.

In many physical situations, the pore pressure, rather than the flux, is imposed at the point of injection. In the appendix A, we studied injection with a fixed pore pressure, and found that the dynamics of constant-pressure injections evolve to be essentially equivalent to those for constant flux. This conclusion applies for as long as a significant pressure signal has not reached a far boundary of the domain, which is also when our constant-flux solutions deviate from self-similar behaviour.

In contrast to this behaviour, in an idealized non-deformable medium the dynamics associated with injection at a fixed pressure must inevitably depend upon the far-field boundary conditions because of the pressure gradients that are immediately set-up. In a deformable medium the pressure signal spreads diffusively and the nearest boundary at $r=r_{edge}$ will have a negligible effect on the dynamics until significant pressure has built up there, which occurs over a time scale of $t \sim \mu_2 r_{edge}^2 / k_0 \tilde{E}$. Example parameter values from In Salah (Rutqvist *et al.* 2010) suggest times of the order of 10^3 days if the nearest boundary or obstacle is at $r_{edge} = 10$ km. Until this time, the dynamics will evolve essentially independently of any far-field conditions, such as faults or fractures in the medium.

Interestingly, if the injected fluid is much less viscous than the ambient fluid (so that $\mu_1/\mu_2 \ll E^{-1/2}$), then the conclusions discussed above break down. In this case (discussed in § 4.3), the injected fluid undercuts the much more viscous ambient fluid which plugs up the medium. The uplift then becomes localized to the position of the injected current rather than diffusing ahead, and the dependence on the parameters change (see table 1). In the context of CO₂ sequestration, however, we estimate that $E > O(10^3)$ while $\mu_1/\mu_2 \approx 1/20$. Thus, although the viscosity ratio is small, it is unlikely to be smaller than $E^{-1/2}$.

In this work we have focused on relatively large values of the stiffness E , since this is the limit appropriate to geophysical contexts. An interesting extension of the model is to consider situations with significant deformation, as in some biological applications. A first step in this direction requires the relaxation of linear poro-elasticity. In such a situation it may also prove necessary to remove the assumption that the fluid and solid phases move together as the overburden lifts up. A pocket of fluid may then float up above the solid matrix to lubricate the overburden, or fluid may drain away underneath as the solid lifts up.

Acknowledgements

D.R.H. is grateful for funding from the PANACEA project and the Killam Foundation. J.A.N. is supported by a Royal Society University Research Fellowship.

Appendix A. Fixed pore pressure at the point of injection

Fluid may be injected at a fixed pore pressure, rather than a fixed flux. In this appendix, we consider injection at a fixed pressure p_I and show that the flow is qualitatively similar to that with a (related) fixed flux Q , until significant uplift has reached a boundary of the domain. As we will show below, infinite pore pressure is required at $r = 0$ to sustain a non-zero flux, which implies that we must consider a finite fixed pressure p_I at a small non-zero radius of injection r_I . In this case, the boundary condition of fixed flux (2.24a) is replaced by

$$p(r = r_I, z = 0) = p_I, \tag{A 1}$$

or, equivalently, using the expression for hydrostatic pressure (2.27) and the balance of normal stress at $z = H$ (2.29),

$$\tilde{p}_I - \rho_2(H - h) - \rho_1 h = E \frac{\Phi - \Phi_0}{1 - \Phi_0}, \quad \text{at } r = r_I, \tag{A 2}$$

where $\tilde{p}_I = p_I - \mathcal{P}$ is the excess imposed pore pressure above the overburden pressure. Equation (A 2) can be combined with the equation for $\Phi(h, H)$ (2.31) to give an implicit relationship between H and h at $r = r_I$, which can be solved iteratively together with the constraint that there is no flux of ambient fluid at $r = r_I$ (2.34b). The corresponding flux $Q(t)$ is given by (2.34a).

Figure 10 compares results from numerical simulations with fixed flux and fixed pressure at $r = r_I$. After an initial transient, simulations with fixed flux have an almost constant pressure \tilde{p}_I (figure 10a), while simulations with fixed pressure have an almost constant flux Q (figure 10b). Figure 10(c,d) emphasizes the correspondence by comparing solutions in which the near-constant flux of the constant-pressure injection was matched by that of an injection with constant flux. In common with most other porous or viscous gravity-current problems, the profiles for fixed flux and non-zero r_I also give very good agreement with the similarity solution.

The dynamics of injection with a fixed pressure can be exposed by an analysis of the equations in the limit $r_I \rightarrow 0$. Provided that the flux of injected fluid remains non-zero in this limit, we require $J_1 \neq 0$ and $J_2 = 0$ from the flux boundary conditions (2.34). These constraints indicate that $h \sim H$ as $r \rightarrow 0$; in other words, as $r_I \rightarrow 0$ the entire layer fills up with injected fluid in some small region close to $r = 0$. The shape of $h \sim H$ close to $r = 0$ can be determined from the equation for the flux (2.33a), which reduces to

$$-rh \left(\rho_1 + \frac{E}{1 - \Phi_0} \frac{\partial \Phi}{\partial h} \right) \frac{\partial h}{\partial r} \rightarrow \frac{Q}{2\pi} \quad \text{as } r \rightarrow 0, \tag{A 3}$$

or

$$h \sim H \sim \left[\frac{Q}{\pi \rho_1} \log \left(\frac{1}{r} \right) \right]^{1/2} \quad \text{as } r \rightarrow 0. \tag{A 4}$$

That is, in some exponentially small region near to $r = 0$, $h \sim H$ diverges. (In the limit $h \rightarrow H \rightarrow \infty$, the gradient of Φ vanishes and $\Phi \rightarrow 1$.) The logarithmic divergence of h as $r \rightarrow 0$ is a generic feature of axisymmetric viscous gravity currents.

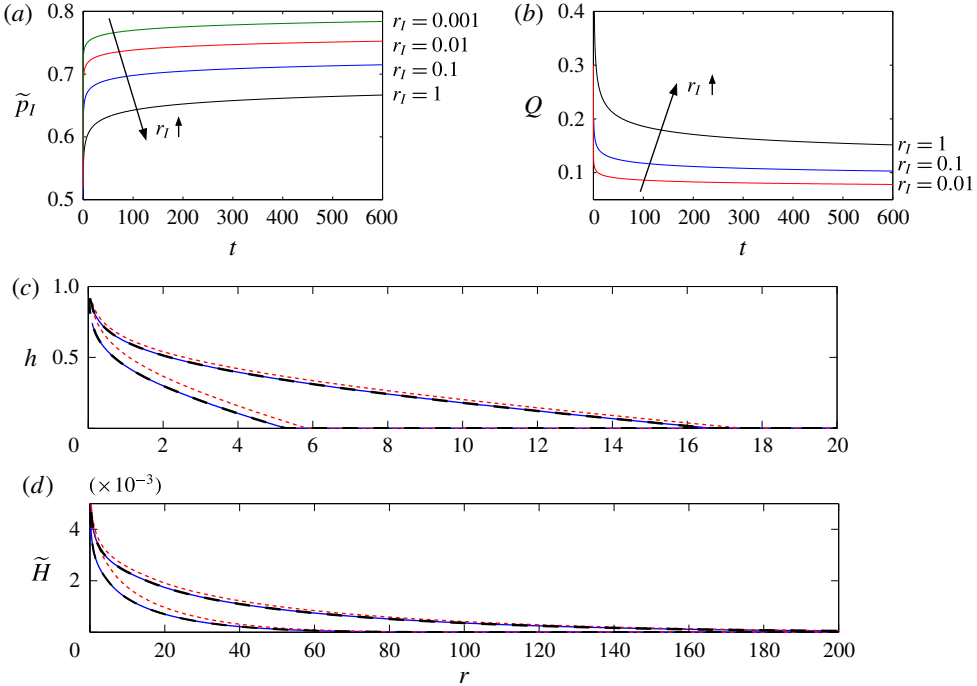


FIGURE 10. (Colour online) Comparison of profiles from simulations with fixed flux Q or fixed pressure \tilde{p}_l at $r = r_l$. (a) The pressure \tilde{p}_l at r_l from simulations with fixed flux $Q = 0.1$, for different $r_l = 1$ as marked. (b) The flux Q at r_l from simulations with fixed pressure $\tilde{p}_l = 0.72$, for different $r_l = 1$ as marked. (c,d) The height $h(r, t)$ of the injected current and the uplift $\tilde{H}(r, t)$, as marked, at times $t = 40$ (leftmost group of curves) and $t = 400$ (rightmost group of curves), with $r_l = 0.1$, for fixed flux $Q = 0.1$ (solid) and fixed pressure $\tilde{p}_l = 0.72$ (short dashed). The simulations with fixed flux agree with the similarity solution (long dashed). The other parameters in these simulations are those given at the start of § 3.

The excess pressure \tilde{p}_l at r_l is given by (A 2) which, using (A 4) and $\Phi \rightarrow 1$, gives

$$\tilde{p}_l \sim \left[\frac{\rho_1 Q}{\pi} \log \left(\frac{1}{r_l} \right) \right]^{1/2} + E \quad \text{as } r_l \rightarrow 0. \tag{A 5}$$

In other words, for sufficiently small values of r_l , the flux and the pressure are directly linked via (A 5), and so flow with a fixed pressure should be the same as flow with the corresponding fixed flux given by (A 5). Equation (A 5) also confirms that the pressure associated with a non-zero flux Q diverges as $r_l \rightarrow 0$.

The agreement of simulations with fixed flux and fixed pressure in figure 10 is not exact, which does not contradict (A 5) because the radius of injection is not exponentially small in those simulations. For the parameter values of those simulations and $h = O(1)$, (A 4) gives estimates of r_l of the order of $r_l \sim e^{-20}$, which is many orders of magnitude smaller than can be readily attained numerically.

In a finite domain, we expect a qualitative difference between the dynamics with a fixed-flux and fixed-pressure boundary conditions once significant uplift has reached the far boundary at $r = r_{edge}$. If the pressure were fixed then the flux would decrease

significantly, whereas if the flux were fixed then the whole system would become pressurized. The diffusive scalings in (4.7) indicate that this change in the dynamics occurs after a (dimensionless) time scale $t \sim r_{edge}^2 / (ME)$.

REFERENCES

- BARABADI, B., NATHAN, R., JEN, K. & WU, Q. 2009 On the characterization of lifting forces during the rapid compaction of deformable porous media. *Trans. ASME J. Heat Transfer* **131** (10), 101006.
- BARRY, S. I. & HOLMES, M. 2001 Asymptotic behaviour of thin poroelastic layers. *IMA J. Appl. Maths* **66**, 175–194.
- BARRY, S. I., MERCER, G. N. & ZOPPOU, C. 1997 Deformation and fluid flow due to a source in a poro-elastic layer. *Appl. Math. Model.* **21** (11), 681–689.
- BEAR, J. 1988 *Dynamics of Fluids in Porous Media*. Dover.
- BEAR, J. & CORAPCIOGLU, M. Y. 1981a A mathematical model for consolidation in a thermoelastic aquifer due to hot water injection or pumping. *Water Resour. Res.* **17** (3), 723–736.
- BEAR, J. & CORAPCIOGLU, M. Y. 1981b Mathematical model for regional land subsidence due to pumping: 1. Integrated aquifer subsidence equations based on vertical displacement only. *Water Resour. Res.* **17** (4), 937–946.
- BEAR, J. & CORAPCIOGLU, M. Y. 1981c Mathematical model for regional land subsidence due to pumping: 2. Integrated aquifer subsidence equations for vertical and horizontal displacements. *Water Resour. Res.* **17** (4), 947–958.
- BISSELL, R. C., VASCO, D. W., ATBI, M., HAMDANI, M., OKWELEGBE, M. & GOLDWATER, M. H. 2011 A full field simulation of the In Salah gas production and CO₂ storage project using a coupled geo-mechanical and thermal fluid flow simulator. *Energy Proc.* **4**, 3290–3297.
- BOAIT, F. C., WHITE, N. J., BICKLE, M. J., CHADWICK, R. A., NEUFELD, J. A. & HUPPERT, H. E. 2012 Spatial and temporal evolution of injected CO₂ at the Sleipner Field, North Sea. *J. Geophys. Res.* **117**, 2156–2202.
- CHARRAS, G. T., MITCHISON, T. J. & MAHADEVAN, L. 2009 Animal cell hydraulics. *J. Cell Sci.* **122** (18), 3233–3241.
- COUSSY, O. 2004 *Poromechanics*. Wiley.
- DETOURNAY, E. & CHENG, A. H.-D. 1993 Fundamentals of poroelasticity. In *Comprehensive Rock Engineering: Principles, Practice and Projects, Vol. II, Analysis and Design Method*, chap. 5., Pergamon.
- EISENBERG, S. R. & GRODZINSKY, A. J. 1987 The kinetics of chemically induced nonequilibrium swelling of cartilage and corneal stroma. *J. Biomed. Engng* **109**, 79–89.
- GIBSON, R. E., SCHIFFMAN, R. L. & PU, S. L. 1970 Plane strain and axially symmetric consolidation of a clay layer on a smooth impervious base. *Q. J. Mech. Appl. Maths* **23** (4), 505–520.
- HUPPERT, H. E. & NEUFELD, J. A. 2014 The fluid mechanics of carbon dioxide sequestration. *Annu. Rev. Fluid Mech.* **46**, 255–272.
- HUPPERT, H. E. & WOODS, A. 1995 Gravity-driven flows in porous layers. *J. Fluid Mech.* **292**, 55–69.
- JENSEN, O. E., GLUCKSBERG, M. R., SACHS, J. R. & GROTBORG, J. B. 1994 Weakly nonlinear deformation of a thin poroelastic layer with a free surface. *J. Appl. Mech.* **61** (3), 729–731.
- LANIR, Y., SAUOB, S. & MARETSKY, P. 1990 Nonlinear finite deformation response of open cell polyurethane sponge to fluid filtration. *J. Appl. Mech.* **57**, 449–454.
- LISTER, J. R., PENG, G. & NEUFELD, J. A. 2013 Viscous control of peeling an elastic sheet by bending and pulling. *Phys. Rev. Lett.* **111**, 154501.
- LYLE, S., HUPPERT, H. E., HALLWORTH, M. A., BICKLE, M. & CHADWICK, A. 2005 Axisymmetric gravity currents in a porous medium. *J. Fluid Mech.* **543**, 293–302.
- MACMINN, C. W., DUFRESNE, E. R. & WETTTLAUER, J. S. 2015 Fluid-driven deformation of a soft granular material. *Phys. Rev. X* **5**, 011020.

- MAK, A. F., LAI, W. M. & MOW, V. C. 1987 Biphasic indentation of articular cartilage I. Theoretical analysis. *J. Biomech.* **20** (7), 703–714.
- MOEENDARBARY, E., VALON, L., FRITZSCHE, M., HARRIS, A. R., MOULDING, D. A., THRASHER, A. J., STRIDE, E., MAHADEVAN, L. & CHARRAS, G. T. 2013 The cytoplasm of living cells behaves as a poroelastic material. *Nat. Mater.* **12** (3), 253–261.
- MOW, V. C., GIBBS, M. C., LAI, W. M., ZHU, W. B. & ATHANASIOU, K. A. 1989 Biphasic indentation of articular cartilage II. A numerical algorithm and an experimental study. *J. Biomech.* **22** (8), 853–861.
- MOW, V. C., HOLMES, M. H. & LAI, W. M. 1984 Fluid transport and mechanical properties of articular cartilage: a review. *J. Biomech.* **17**, 377–394.
- NORDBOTTEN, J. M. & CELIA, M. A. 2006 Similarity solutions for fluid injection into confined aquifers. *J. Fluid Mech.* **561**, 307–327.
- ONUMA, T. & OHKAWA, S. 2009 Detection of surface deformation related with CO₂ injection by DInSAR at In Salah, Algeria. *Energy Proc.* **1**, 2177–2184.
- PARKER, K. H., MEHTA, R. V. & CARO, C. G. 1987 Steady flow in porous, elastically deformable materials. *J. Appl. Mech.* **54**, 794–799.
- PEGLER, S. S., HUPPERT, H. E. & NEUFELD, J. A. 2014 Fluid injection into a confined porous layer. *J. Fluid Mech.* **745**, 592–620.
- PHILLIPS, O. M. 2009 *Geological Fluids Dynamics*. Cambridge University Press.
- RINGROSE, P., ATBI, M., MASON, D., ESPINASSOUS, M., MYHRER, Ø., IDING, M., MATHIESON, A. & WRIGHT, I. 2009 Plume development around well KB-502 at the In Salah CO₂ storage site. *First Break* **27** (1), 85–89.
- RINGROSE, P. S., MATHIESON, A. S., WRIGHT, I. W., SELAMA, F., HANSEN, O., BISSELL, R., SAOULA, N. & MIDGLEY, J. 2013 The In Salah CO₂ storage project: lessons learned and knowledge transfer. *Energy Proc.* **37**, 6226–6236.
- RUCCI, A., VASCO, D. W. & NOVALI, F. 2013 Monitoring the geologic storage of carbon dioxide using multicomponent sar interferometry. *Geophys. J. Intl* **193**, 197–208.
- RUTQVIST, J. 2012 The geomechanics of CO₂ storage in deep sedimentary formations. *Geotech. Geol. Engng* **30**, 525–551.
- RUTQVIST, J., VASCO, D. W. & MYER, L. 2010 Coupled reservoir-geomechanical analysis of CO₂ injection and ground deformations at In Salah, Algeria. *Intl J. Greenh. Gas Control* **4**, 225–230.
- SACHS, J. R., GLUCKSBERG, M. R., JENSEN, O. E. & GROTBORG, J. B. 1994 Linear flow and deformation in a poroelastic disk with a free surface. *J. Appl. Mech.* **61** (3), 726–728.
- SIMON, B. R., LIABLE, J. P., PFLASTER, D., YUAN, Y. & KRAG, M. H. 1996 A poroelastic finite element formulation including transport and swelling in soft tissue structure. *Trans. ASME J. Biomech. Engng* **118**, 1–9.
- WANG, H. F. 2000 *Theory of Linear Poroelasticity with Applications to Geomechanics and Hydrogeology*. Princeton University Press.
- ZHANG, W. 2013 Density-driven enhanced dissolution of injected CO₂ during long-term CO₂ storage. *J. Earth Syst. Sci.* **122**, 1387–1397.